This document is confidential and is proprietary to the American Chemical Society and its authors. Do not copy or disclose without written permission. If you have received this item in error, notify the sender and delete all copies.

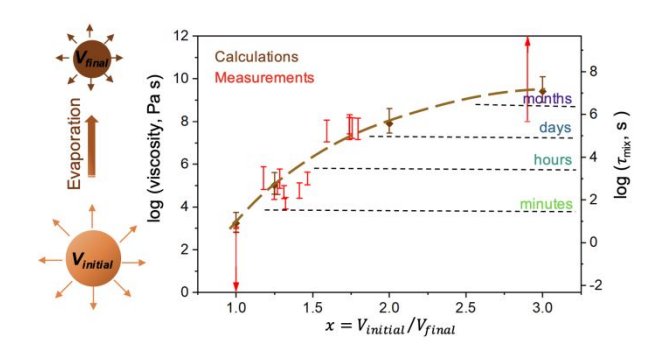
Molecular Insights into Gas-Particle Partitioning and Viscosity of Atmospheric Brown Carbon.

Journal:	Environmental Science & Technology
Manuscript ID	es-2024-05650u.R3
Manuscript Type:	Article
Date Submitted by the Author:	n/a
Complete List of Authors:	Xie, Qiaorong; Purdue University, Chemistry Gerrebos, Nealan; The University of British Columbia, Department of Chemistry Calderon-Arrieta, Diego; Purdue University, Chemistry Morton, Isaac; Purdue University College of Engineering, Chemical Engineering Halpern, Emily; Purdue University Department of Chemistry, Li, Chunlin; Weizmann Institute of Science, Department of Earth and Planetary Sciences Zeng, Mei Fei; University of British Columbia, Department of Chemistry Bertram, Allan; University of British Columbia, Chemistry Rudich, Yinon; Weizmann Institute of Science, Earth and Planetary Sciences Laskin, Alexander; Purdue University, Chemistry

SCHOLARONE™ Manuscripts

- 1 Molecular Insights into Gas-Particle Partitioning and Viscosity of Atmospheric
- 2 Brown Carbon.
- 4 Qiaorong Xie,¹ Nealan G. A. Gerrebos,⁴ Diego Calderon-Arrieta,¹ Isaac S. Morton,³
- 5 Emily R. Halpern, 1 Chunlin Li, 5 Mei Fei Zeng, 4 Allan K. Bertram, 4 Yinon Rudich, 6
- 6 Alexander Laskin^{1,2*}
- 8 ¹ Department of Chemistry, ² Department of Earth, Atmospheric, and Planetary Sciences,
- ³Davidson School of Chemical Engineering, Purdue University, West Lafayette, Indiana, 47907,
- 10 United States
- ⁴Department of Chemistry, University of British Columbia, Vancouver, V6T 1Z1, BC, Canada
- ⁵College of Environmental Science and Engineering, Tongji University, Shanghai 200072, China
- ⁶Department of Earth and Planetary Sciences, Weizmann Institute of Science, Rehovot 76100,
- 14 Israel
- **Corresponding author: alaskin@purdue.edu

18 TOC Art



ABSTRACT. Biomass burning organic aerosol (BBOA), containing brown carbon chromophores, plays a critical role in atmospheric chemistry and climate forcing. However, the effects of evaporation on BBOA volatility and viscosity under different environmental conditions remain poorly understood. This study focuses on the molecular characterization of laboratory-generated BBOA proxies from wood pyrolysis emissions. The initial mixture, "pyrolysis oil (PO₁)," was progressively evaporated to produce more concentrated mixtures (PO_{1,33}, PO₂, and PO₃) with volume reduction factors of 1.33, 2, and 3, respectively. Chemical speciation and volatility were investigated using temperature-programmed desorption combined with direct analysis in real-time ionization and high-resolution mass spectrometry (TPD-DART-HRMS). This novel approach quantified saturation vapor pressures and enthalpies of individual species, enabling the construction of volatility basis set distributions and the quantification of gas-particle partitioning. Viscosity estimates, validated by poke-flow experiments, showed a significant increase with evaporation, slowing particle-phase diffusion and extending equilibration times. These findings suggest that highly viscous tar ball particles in aged biomass burning emissions form as semivolatile components evaporate. The study highlights the importance of evaporation processes in shaping BBOA properties, underscoring the need to incorporate these factors into atmospheric models for better predictions of BBOA aging and its environmental impact.

- Keywords. Volatility and viscosity; atmospheric brown carbon; biomass burning organic aerosol,
 gas-particle partitioning; non-reactive evaporation, TPD-DART-HRMS.
- Synopsis. Molecular characterization of complex biomass burning organic aerosol (BBOA)
 mixtures enables quantitative analysis of gas-particle partitioning of aerosol components and
 assessment of viscosity and diffusion within the particle phase.

INTRODUCTION

Biomass burning organic aerosol (BBOA), emitted from wildfires and agricultural burns, contains a substantial amount of gaseous and particulate light-absorbing material known as brown carbon (BrC)¹⁻⁴, contributing to a significant climate warming effect. Exploring the formation, transformation, and removal pathways of BBOA is crucial to understand their impact on air quality and Earth's climate, 5, 6 particularly as wildfires become more frequent and widespread globally. 7, ⁸ Atmosp⁴heric ageing alters the composition and optical properties of BrC through various chemical and physical processes, thereby influencing atmospheric chemistry and climate. The chemically complex components of BrC can be removed from BBOA through evaporation and reaction chemistry, leading to the production of more volatile species. 10 Various multi-phase reactions can darken BrC aerosols within hours of emission, while photobleaching and oxidative whitening may occur a day or more later. 9, 10 However, the influence of non-reactive evaporation of BBOA remains underappreciated, and little is known about how evaporation affects particle chemical composition and physical properties. 11, 12 Both volatility and viscosity are important properties of BBOA, as they influence essential processes such as the dynamics of gas-particle partitioning and organic aerosol evolution. 13 Recent research indicates that BBOA darkens upon volatilization, thereby amplifying its BrC optical absorbance. 11 Nonetheless, quantifying the impact of evaporation on volatility and viscosity properties of BBOA remains incomplete. Atmospheric BBOA and its BrC components comprise a diverse mixture of individual species existing in a dynamic equilibrium between gaseous and particulate phases. Through various atmospheric transformations, these complex components undergo multiple processes, with the partitioning of these components between gas and particle phases being central. 14, 15 Volatility, defined by saturation vapor pressure, is a fundamental property governing the gas-particle

partitioning of individual BBOA components, thereby influencing their atmospheric fate. ^{16, 17} The volatility of species is influenced by intrinsic properties such as molecular weights, chemical structures, and intra-molecular forces, as well as external conditions of temperature, pressure, humidity, and total organic mass loading. ¹⁸⁻²² However, measuring the volatility values of individual components in BBOA mixtures is challenging due to their chemical complexity and diversity. This complexity complicates the construction and assessment of the corresponding volatility basis sets (VBS) used to model gas-particle partitioning. ¹⁶

Recent advances have facilitated this task. A novel experimental approach integrates thermal evaporation of organic aerosol (OA) samples using a temperature programmed desorption (TPD) stage with the direct analysis in real time (DART) ionization source and high-resolution mass spectrometer (HRMS). This method enables the direct measurement of the apparent saturation vapor pressures (${}^{i}p_{T}^{*}$, Pa) of individual species (i) across a broad temperature (T, K) range.²³ Additionally, these measurements provide values of apparent transition enthalpies (${}^{i}\Delta H^{*}$, kJ/mol), characterizing individual organic molecules as they undergo evaporation or sublimation. Using the records of ${}^{i}p_{T}^{*}$ converted into saturation mass concentration (${}^{i}C_{T}^{*}$, $\mu g \cdot m^{-3}$) and ${}^{i}\Delta H^{*}$ values obtained for individual components of OA, the VBS distributions are constructed. These distributions facilitate a quantitative assessment of the gas-particle partitioning of aerosol components, aiding in the prediction of their behavior and evolution in the atmosphere.²⁴

Higher viscosity is associated with slower diffusion, longer characteristic mixing times, and inhibited multiphase chemistry within aerosol mixtures, all of which are influenced by their composition and environmental conditions.^{25, 26} Quantifying particle viscosity is crucial for accurately predicting the phase state of BBOA particles, although viscosity measurements are very

challenging.²⁷ However, the impact of evaporation on temperature- and relative humidity (RH)-dependent BBOA viscosity has not been previously documented.

In this study, samples of BBOA proxies were collected from emissions generated by the pyrolysis of wood chips in a laboratory setup. Afterwards, samples with varying degrees of evaporation were obtained. The TPD-DART-HRMS experiments were employed to measure the values of ${}^{i}\Delta H^{*}$ and ${}^{i}C_{T}^{*}$ of individual components, along with their corresponding mass fraction values. Subsequently, VBS distributions were constructed to quantitatively assess the equilibrium gas-particle partitioning of BBOA under atmospherically relevant conditions, including a range of total organic mass loadings (tOM, $\mu g \cdot m^{-3}$) and temperatures (T, K). The viscosity values of BBOA mixtures were estimated using the VBS-based prediction of the chemical composition of particle-phase components. These calculated values were then compared with viscosity measurements employing poke-flow experiments to demonstrate their utility and explore viscosity variations during the evaporation processes in the atmosphere.

EXPERIMENTAL AND ANALYSIS METHODS

Generation of BBOA and non-reactive evaporation processes. Smoke emissions resulting from the pyrolysis of hardwood pellets, which mimic the chemical and optical properties of ambient biomass burning aerosols, ^{12, 28} were collected using a water-circulating condenser, operated at *T* =293 K. The collected liquid condensate naturally separated into immiscible "aqueous" and "oily" fractions in a separatory funnel. For this study, the initial oily fraction, designated as wood Pyrolysis Oil (PO₁), was isolated and employed as a proxy for BBOA. Three aliquots of PO₁, each with a volume of 10 mL, underwent thermal treatment at 350 °C with a flow of N₂ gas passing over the mixtures to facilitate the evaporation of their volatile components for varying durations.

Additionally, tests were performed using PO₁ evaporation in a vacuum chamber to confirm that compositional changes in the heated samples were attributed to the removal of volatile constituents rather than chemical reactions facilitated by the thermal treatment.¹¹ The resulting evaporated samples were denoted as PO_x, where x represents the ratio of the initial volume to the final volume after evaporation ($x = V_{initial} / V_{evaporated}$). For example, if 50% of the initial volume of PO₁ remained after a 40 min evaporation process, it would be referred to as PO₂. In this study, PO₁, PO_{1,33}, PO₂, and PO₃ were utilized. Detailed information on the generation and evaporation methods of PO_x preparations are described in our previous reports.^{11, 12, 28}

TPD-DART-HRMS experiments and data analysis. The detailed description of the TPD-DART-HRMS experimental setup, its operational procedures, the associated methodology for quantitative data analysis, the construction of VBS distributions, and their validation results have been thoroughly documented in our previous publications.^{23, 24} Briefly, small portions of the PO_x bulk samples (~10 µL) were individually placed onto a copper stub heated during each TPD experiment. The temperature ramping profile started at 298 K, held for 0.4 min, followed by a linear ramp at a rate of 70 K min⁻¹ to 773 K, and then maintained at the final temperature for 2 min. The temperature profile is shown in Figure S2. The DART ionization source, interfaced with the Q-Exactive HF-X Orbitrap mass analyzer (operated at mass resolution of m/ Δ m $\sim 240,000$ at 200 m/z), dynamically ionized the gas-phase species degassing from the PO_r samples during the TPD experimental runs. Progression of the high-resolution mass spectra was recorded to identify individual components. Molecular formulas were assigned based on the ions detected in negative mode, (-)DART-HRMS in the m/z range of 100–1000 Da, with constraints of $C_{1-40}H_{1-100}O_{1-25}N_{0-1}$ ₁ and mass tolerance of ± 2.0 ppm.²⁹ In these experiments, the (-)DART ionization mechanism led to the formation of deprotonated molecules [M-H]⁻ and radical anions M⁻*. Consequently, the

apparent saturation vapor pressure ${}^{i}p_{T}^{*}$ (Pa) of each component (i) as a function of temperature (T) are determined using the Clausius-Clapeyron equation (Eq. 1). 30 The values of saturation vapor pressure are then converted to saturated mass concentrations ${}^{i}C_{T}^{*}$ (µg m $^{-3}$) based on the ideal gas equation (Eq. 2). These calculations require input values of ${}^{i}T_{max}^{*}$, ${}^{i}\Delta H^{*}$, ${}^{i}p_{max}^{*}$, and molecular weight of $C_{x}H_{y}O_{z}$ species i (${}^{i}MW$), all inferred from the TPD-DART-HRMS records. 23 , ${}^{24}{}^{i}T_{max}^{*}$ corresponds to the peak ion intensity in the extracted ion thermograms of individual species. The values of ${}^{i}\Delta H^{*}$ are derived from the slope of Arrhenius plots as discussed below. The reference vapor pressure ${}^{i}P_{max}^{*}$ of the individual species (i) is estimated by assuming the stoichiometry of its formal combustion oxidation reaction, as described in our earlier publication. ${}^{23}R$ denotes the molar gas constant with value of 8.3145 J mol $^{-1}$ K $^{-1}$.

$${}^{i}p_{T}^{*} = {}^{i}p_{T_{max}}^{*} \times exp\left[\left(-\frac{{}^{i}\Delta H^{*}}{R}\right)\left(\frac{1}{T} - \frac{1}{T_{max}^{*}}\right)\right] \tag{1}$$

$${}^{i}C_{T}^{*} = \frac{{}^{i}p_{T}^{*} \times 10^{9} \times {}^{i}MW}{RT}$$
 (2)

Volatility basis sets constructions. The VBS framework, which segments the volatility spectrum of BBOA components into distinct bins, 16,31 is utilized to characterize the entire range of saturation vapor pressures of PO_x components based on their $^i\Delta H^*$, $^iC_T^*$ and mass fraction values of individual components, as described in our previous publication. 24 Briefly, individual species i are grouped into a series of $(logC^*)_j$ bins, where j represents individual bins marked by integer values. The relative heights (H_j) of VBS bins j are calculated as the sum of the molar fractions of species contained within each bin, normalized to the sum of heights across all bins, expressed by the following equation (Eq. 3):

$$H_j = \frac{\left[\sum_i (S_i \times A_i \times MW_i)\right]_j}{\sum_j \left[\sum_i (S_i \times A_i \times MW_i)\right]_j}, \text{ where } \sum_j H_j = 1$$
 (3)

where A_i is the molar fraction of species i, proportional to the area under its TPD-HRMS thermogram; MW_i and S_i are the molecular weight and sensitivity of species i (Figure S1), respectively.

The particle-phase mass fractions of aerosolized PO_x mixtures for each individual bin j is then computed using the constructed VBS distributions. This calculation considers different values of the total organic mass (tOM) loadings in the air (e.g. 1, 10, 100, etc. μ g m⁻³) with the following equation (Eq. 4):

$$X_j^P = H_j \times \frac{C_{tOM}}{C_{tOM} + {}^iC_T^*} \tag{4}.$$

Viscosity calculations. The glass transition temperature $(T_{g,i})$ of each organic component (i) is estimated using a parameterization method based on the number of carbon (n_C) , hydrogen (n_H) , and oxygen (n_O) atoms in the corresponding elemental formula. The estimation employs the equation 5 along with parameter values for n_C^0 , b_C , b_H , b_{CH} , b_O , and b_{CO} listed in Table S1.³²

$$T_{g,i} = (n_C^o + \ln(n_C))b_C + \ln(n_H)b_H + \ln(n_C)\ln(n_H)b_{CH} + \ln(n_O)b_O + \ln(n_C)\ln(n_O)b_{CO}$$
(5)

The glass transition temperature $(T_g(\omega_{org}))$ of PO_x mixtures in a form of aerosolized particles containing water is estimated using the Gordon-Taylor equation (Eq. 6):^{32, 33}

$$T_g(\omega_{org}) = \frac{(1 - \omega_{org})T_{g,w} + \frac{1}{K_{GT}}\omega_{org}T_{g,org}}{(1 - \omega_{org}) + \frac{1}{K_{GT}}\omega_{org}}$$
(6)

Here, the ω_{org} is the organic mass fraction in the aerosolized PO_x particles containing water, computed as $\omega_{org} = m\text{PO}_x / (m\text{PO}_x + m\text{H}_2\text{O})$, where $m\text{PO}_x$ and $m\text{H}_2\text{O}$ are particle phase masses of PO_x and water, respectively. For each of the environmental conditions of T (K) and tOM (µg·m⁻³) considered, $m\text{PO}_x$ is calculated by summing the particle-phase mass fractions across all bins j comprising the corresponding VBS distribution. Values of $m\text{H}_2\text{O}$ are subsequently calculated for

PO_x-water aerosol mixtures equilibrated at various RH using the modified Kohler theory,³⁴ assuming an effective hygroscopicity parameter $\kappa = 0.057 \pm 0.07$, as reported for BBOA in the literature.³⁵ The glass transition temperature $(T_{g,org})$ of the the aerosolized PO_x mixture is calculated as $T_{g,org} = \sum_i \omega_i T_{g,i}$, where ω_i represents the mass fraction of each component i present in the VBS-calculated particle phase.³⁶ The glass transition temperature of pure water $(T_{g,w})$ and the Gordon-Taylor constant (k_{GT}) were set as 136 K and 2.5, respectively.³⁷ The same Gordon-Taylor constant was used for $T_g(\omega_{org})$ calculations for each of the PO_x mixtures. Additionally, $T_g(\omega_{org})$ values of PO_x mixtures were calculated from experimental values of C^*_{298K} using a separate parameterization approach,³⁸ as detailed in supplementary note 1 (Supporting Information).

The viscosity (η , Pa·s) of individual organic components and their mixtures can be derived from $T_{g,i}$ and $T_{g,org}$, respectively, using the Vogel-Tammann-Fulcher (VTF) equation (Eq. 7):³²

$$log\eta = -5 + 0.434 \frac{T_0 D}{T - T_0} \tag{7}$$

where T_0 is the Vogel temperature ($T_0 = 39.17 \times T_g/(D + 39.17)$) and D is the fragility parameter, assumed to be 10 when $T_g < T$. Finally, viscosity values derived for mixtures of interest are used to calculate their corresponding diffusion coefficients (D_b) using the Stokes-Einstein equation (Eq. 8):

$$D_{\rm b} = \frac{kT}{6\pi a\eta} \tag{8}$$

where k is the Boltzmann constant (1.38×10⁻²³ J K⁻¹) and a is the effective molecular radius approximated as 1nm.^{37, 39}

The mixing time axes (τ_{mix}, s) were calculated with the following equation (Eq. 9):⁴⁰

$$\tau_{mix} = \frac{d_p^2}{4\pi^2 D_b} \tag{9}$$

where d_p is the particle diameter.

Viscosity measurements. Viscosities were measured using the poke-flow method. 41, 42 PO₁ was deposited on 12 mm glass microscope cover slips by dipping the blunt end of a 0.25 mm diameter needle in PO₁ and then tapping the needle against the cover slip, leaving behind spherical-cap droplets with base diameters ranging from 60 to 120 µm. The cover slips have been coated with a hydrophobic/oleophobic coating (Fluoropel-800, Cytonix) to facilitate the spherical shape of the droplets. The samples were placed in a temperature-controlled flow cell, warmed to 80°C under N₂ gas, and maintained at this temperature to facilitate partial evaporation of the droplets. Before and after heating, the volume of each droplet was measured using a confocal laser-scanning fluorescence microscope (Axio Observer LSM 510MP, Zeiss). The $x=V_{initial}/V_{final}$ of the droplets ranged from 1.2 to 2.9 after heating. Poke-flow viscosity measurements were then carried out as described in detail elsewhere. 41, 43 In short, the samples were placed in a flow cell located above an inverted microscope and with a fine needle (0.25 mm diameter, 13561-10 Ted Pella) inserted through the top of the flow cell. The samples were conditioned to dry conditions by leaving them under a flow of dry zero-air in the dark for 1 hour before poking. Using a micromanipulator, the needle was lowered into the center of a PO_x droplet, creating a circular deformation. Upon rapid removal of the needle, the PO_x flowed back into the hole to restore its original geometry. The time taken for the hole to close (the recovery time) was then recorded. The initial and final geometries of the droplets and the recovery times were then used in a COMSOL Multiphysics microfluidics simulation to find the lower and upper limits of the droplets' viscosities. Parameters used in the simulations are listed in Table S2. When a droplet was highly viscous, the hole did not recover at all after >12 hours and only a lower limit to the viscosity was established. If the hole closed faster than the camera could capture, then only an upper limit to the viscosity was reported.

RESULTS AND DISCUSSION

Figure 1 illustrates representative results obtained from the TPD-DART-HRMS experiments with PO₁ and PO₃ mixtures, alongside the corresponding data processing workflow. In each experiment, the progression of high-resolution mass spectra is recorded as a TPD thermogram (Figures 1a and 1b). The accurate mass measurements allow for untargeted identification of individual components through assignments of their elemental formulas. Components that evaporate below 300 °C comprise of low-volatility and semi-volatile species, while the extremely low-volatility species that remain after heating at 300 °C are referred to as non-refractory components. 44, 45 Based on the TPD mass spectra progression, evaporated components of PO₁ and PO₃ samples were detected, with their elemental composition identified, as further detailed in Figures S2 and S3. The distinctions between the PO₁ and PO₃ components are primarily attributable to different relative intensities of HRMS features corresponding to low-volatility and semi-volatile compounds. Specifically, the PO₁ sample exhibits prominent features of relatively low molecular weight species within a mass range of 100-200 Da, whereas the PO₃ sample manifests additional abundant species with higher masses of 150–300 Da. Additionally, organic components within PO₃ exhibit higher fractions of species characterized by longer carbon chain length and lower hydrogen saturation compared to the PO₁ sample (Figure S3).⁴⁶ These observations suggest that the evaporation process primarily depletes low molecular weight components with high saturation levels. Conversely, higher molecular weight species (>150 Da) exhibit minimal alterations upon evaporation, indicating their extremely low volatility and consequent persistence within the particulate matter upon aerosolization.

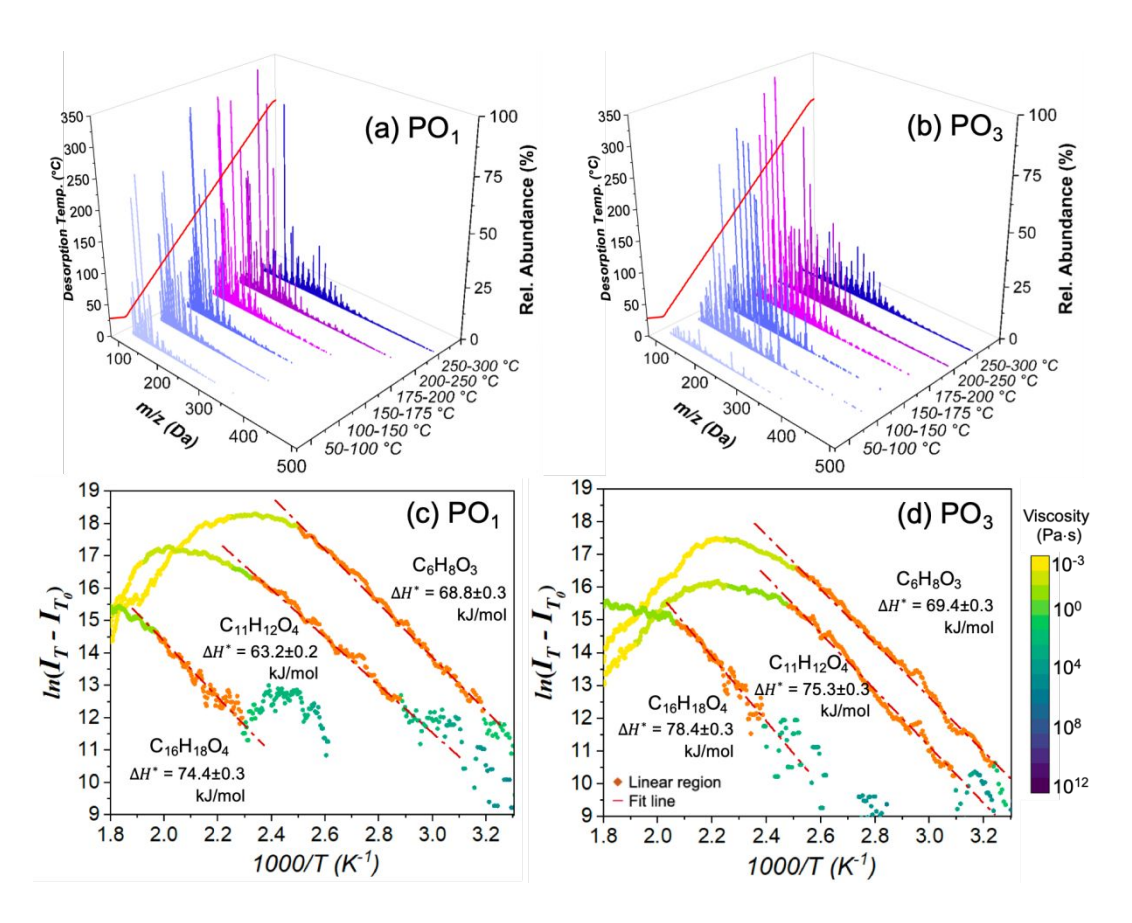


Figure 1. (a-b) Progression of (–)DART-HRMS spectra of PO₁ (a) and PO₃ (b) samples averaged over annotated temperature ranges of the TPD experiment. The temperature profile (red line) is shown along the second y-axis of the plot. The relative abundances of the individual peaks are arbitrarily scaled to the cubic root of the corresponding MS peaks relative intensities to facilitate the comparison. (c-d) The Arrhenius plots of $ln(I_T - I_{T0})$ versus I/T (K-1) of three selected species of $C_6H_8O_3$, $C_{II}H_{I2}O_4$, and $C_{I6}H_{I8}O_4$. Orange symbols denote linear regions used to fit (red dashed lines) the data using Clausius—Clapeyron equation and calculate the apparent enthalpies of solid-to-gas transitions, shown in legends. The color scale reflects viscosity values calculated for each species as a function of temperature during the TPD run.

The apparent enthalpies ${}^{i}\Delta H^{*}$ characterizing the transition of individual species from particle to gas phase are determined from the slope of Arrhenius plots, plotting the logarithm of ion intensity $(ln\ (I_{T}-I_{T0}))$ versus the inverse temperature (I/T), based on the extracted ion signal recorded during the TPD run.²³ Figures 1c and 1d illustrate examples of the ${}^{i}\Delta H^{*}$ values derived from TPD thermograms for three selected common species of $C_{6}H_{8}O_{3}$, $C_{II}H_{I2}O_{4}$, and $C_{I6}H_{I8}O_{4}$ between PO₁ and PO₃ mixtures. The viscosity calculations indicate that at the onset temperatures when each

species starts to evaporate, their viscosity is at the lower values of $<10^1$ Pa·s, indicative of oily liquids. As temperatures increase, their viscosity gradually decreased, eventually reaching values of 10⁻³ Pa·s, comparable to that of water.³⁷ This observation indicates that extensive evaporation of individual PO_x components occurs as they liquefy, implying low kinetic limitations for the evaporated analyte molecules prior to their arrival to the ionization source. In our previous work, ²⁴ it has been demonstrated that near-equilibrium conditions are achieved at each TPD stage, allowing for the assumption that the linear sections of the Arrhenius plots can be used to derive the apparent enthalpies ${}^{i}\Delta H^{*}$ characteristic of condensed-to-gas phase transitions of individual species i. In the previous study, 23 the validity of this assumption was confirmed by measuring ${}^{i}\Delta H^{*}$ and ip_T^* values for a set of carboxylic acids standards, showing close agreement with literature data. Notably, the temperature range of the Arrhenius plots used to determine the ${}^{i}\Delta H^{*}$ values of identified species was below 200 °C (473 K), where most organic species remain stable. 47-49 with the exception of peroxides, which may decompose above ~80 °C (353 K).⁵⁰ At elevated temperatures above 300 °C, thermal decomposition products of organic species are observed in our experiments. However, the apparent ${}^{i}\Delta H^{*}$ and ${}^{i}p_{T}^{*}$ values of species detected at these high temperatures suggest that they are derived from extremely low volatility precursors that do not partition into the gas phase under atmospherically relevant conditions. Consequently, these species have a minimal impact on the gas-phase partitioning.

The apparent ${}^{i}\Delta H^{*}$ values determined for the species $C_{6}H_{8}O_{3}$, $C_{11}H_{12}O_{4}$, and $C_{16}H_{18}O_{4}$ detected in the PO₁ mixture are 68.8 ± 0.3 kJ mol⁻¹, 63.2 ± 0.2 kJ mol⁻¹, and 74.4 ± 0.3 kJ mol⁻¹, respectively. The ${}^{i}\Delta H^{*}$ values measured for the same species detected in the PO₃ mixture are 69.4 ± 0.3 kJ mol⁻¹, 75.3 ± 0.3 kJ mol⁻¹, and 78.4 ± 0.3 kJ mol⁻¹, correspondingly. Both experiments exhibit the expected trend of higher enthalpy values for larger molecules. Additionally, the enthalpy values

of individual species observed in the PO₃ experiment are consistently higher than those reported in the PO₁ experiment. The observed disparities in the apparent enthalpies of individual species sharing the same elemental formulas, though reported separately in different PO_x experiments, likely result from a combination of factors. For instance, differences in the number and molar ratios of isomers present in the progression of the PO_x samples could contribute to these variations. Additionally, stronger Raoult matrix effects may play a role, constraining the evaporation of species from mixtures containing larger organic molecules, which is consistent with the higher enthalpies reported in the PO₃ experiment. Consequently, the derived saturation mass concentrations (${}^{i}C_{T}^{*}$) showed a general downward trend with increasing molecular weight (Figure S4).

The saturation mass concentrations (${}^{i}C_{T}^{*}$) across a wide range of experimental temperatures are determined from the apparent ${}^{i}\Delta H^{*}$ values obtained from the experiments, enabling the construction of VBS distributions at varying temperatures. 24 Figures 2(a–c) depict the alterations in the VBS distribution of compounds in PO₁, considering the process of atmospheric cooling exemplified for the aerosol-gas system of total mass loading of $tOM = 1000 \, \mu g \, m^{-3}$, calculated at decreasing temperatures of 473 K, 373 K, and 298 K, respectively. The progression of these VBS plots allows for a quantitative assessment of the gas-particle partitioning in the biomass burning plume as it travels away from the high-temperature emission zone. Assuming the case scenario of tOM=1000 $\mu g \, m^{-3}$, almost all (>92% by mass) of the compounds in PO₁ exist in the gas phase at temperatures higher than 473 K, where saturation mass concentrations of all individual organic species in the plume will be within the ranges of volatile organic compounds (VOC), $6 < log (C^*, \mu g \, m^{-3})$, and intermediate volatility organic compounds (IVOC), $2 < log (C^*, \mu g \, m^{-3}) \le 6$. As the temperature decreases to 373 K, around 37% of the PO₁ partitions into the particle phase, driven

by the species for which saturation mass concentrations are lowered down to the range of semivolatile organic compounds (SVOC), $-2 < log (C^*, \mu g m^{-3}) \le 2$, and low-volatility organic compounds (LVOC), $-6 < log (C^*, \mu g m^{-3}) \le -2.51$ Further decrease of temperature to common ambient 298 K drives 79% of the PO₁ species by mass into the particle phase, where significant fractions of PO₁ species start to exhibit saturation mass concentrations in the range of extremely low volatility organic compounds (ELVOC), $\log (C^*, \mu g m^{-3}) \le -6$. Upon further reduction of the temperature to 278 K, approximately 89% of the PO₁ compounds partition into the particle phase. Figures 2(a-c) exemplify that decreasing temperatures shift the VBS distribution towards lower volatility, resulting in larger fractions of BBOA components partitioning into the particle phase. Importantly, the extent of gas-particle partitioning can now be quantitatively assessed based on the bottom-up constructed VBS distributions derived from the temperature dependent values of ${}^{i}C_{T}^{*}$ obtained for individual species i in the TPD-DART-HRMS experiments. However, when calculating VBS distributions at temperatures beyond the experimentally observed Arrhenius range, caution is required. The assumption that ${}^{i}\Delta H^{*}$ values remain temperature-independent may not hold true at significantly extrapolated temperatures.

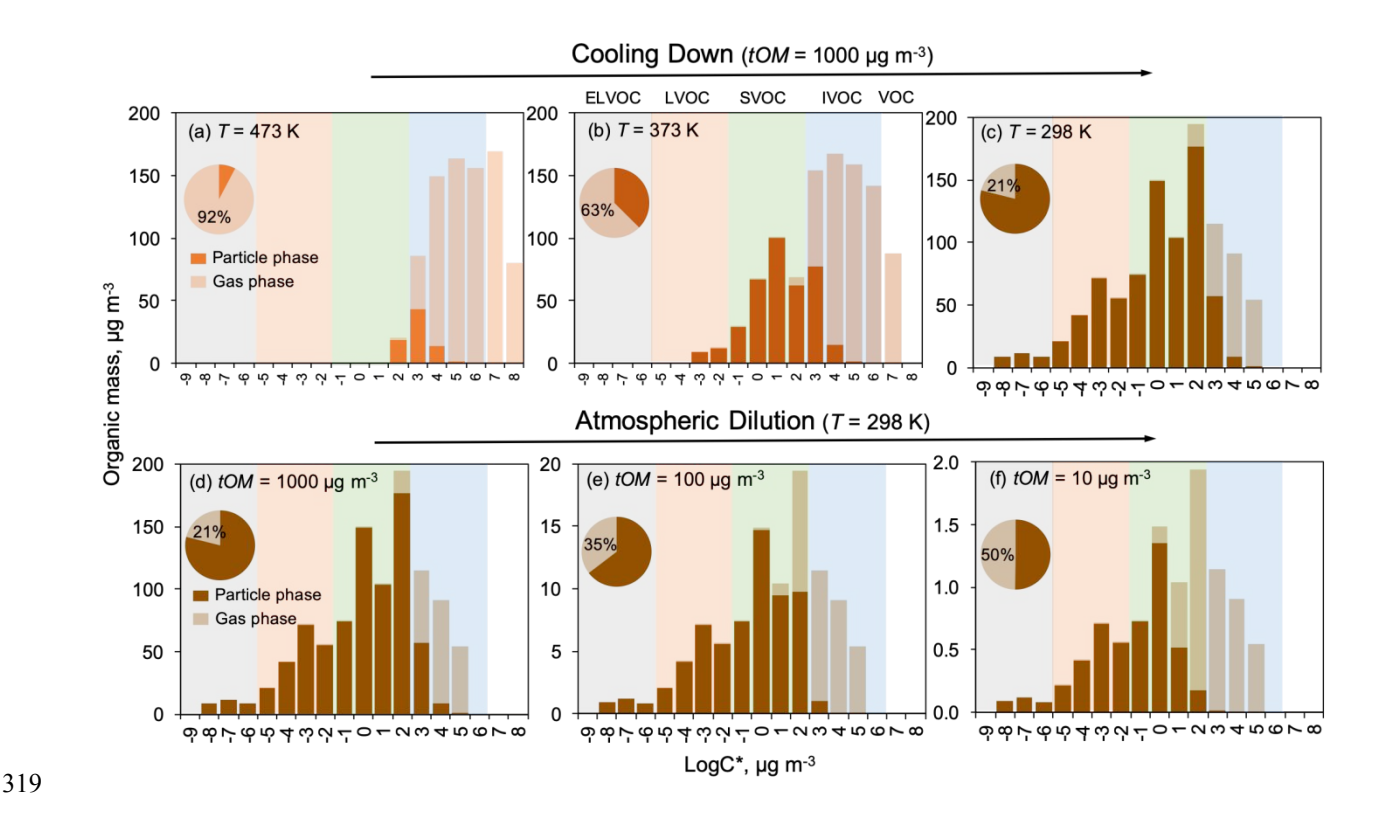


Figure 2. (a–c) Volatility basis set (VBS) distributions for components of the PO₁ mixture considering an atmospheric cooling down process of biomass burning emissions exemplified by decreasing temperatures (473 K, 373 K, and 298 K) and a constant organic mass (*tOM*) loadings of 1000 μg m⁻³. (d–f) VBS distributions for components of the PO₁ sample mixture considering atmospheric dilution exemplified by decreasing values of *tOM* loadings (1000, 100, and 10 μg m⁻³) and a temperature of 298 K. Light colors denote the portions of PO₁ components capable of gas-phase partitioning under these conditions. Pie charts depict the estimated mass fractions percent of gas-phase and particle-phase species summed across all VBS bins.

Gas-particle partitioning in the biomass burning plume is additionally influenced by dilution upon dispersal into the background atmosphere. In addition to the atmospheric temperature, the total mass loadings, which vary during air transport, play a crucial role in shaping the gas-particle partitioning of BBOA compounds. Figures 2(d–f) illustrate the transition between the gas-phase and particle-phase fractions of the PO₁ mixture, as inferred from the VBS distributions constructed for an ambient temperature of 298 K. This transition is exemplified by a progression of decreasing total organic mass loadings of tOM = 1000, 100, and 10 μ g m⁻³, respectively, considering the

process of atmospheric dilution. Near biomass burning sources, concentrations of all emissions are very high, e.g. 1000 μg m⁻³, ⁵² where 80% of PO₁ compounds remain in the particle phase, with the remaining 20% released into the gas phase. As the atmospheric dilution progresses, the *tOM* loadings gradually diminish, and more particle-phase compounds partition into the gas phase. Considering the *tOM* loadings of 100 μg m⁻³, 35% of PO₁ compounds transition into the gas phase. With further dilution during prolonged atmospheric transport where *tOM* loadings would decrease to 10 μg m⁻³, 50% of PO₁ components shift to the gas phase, leaving the other half in the particle phase. A comparison of the VBS distributions for the PO₁ and PO₃ mixtures with those of ambient BBOA from selected field studies^{53, 54} is provided in Figure S5. The VBS distribution of the PO₃ mixture shows significant similarity to that of ambient BBOA, suggesting it may represent a substantially aged aerosol. These observed similarities highlight the potential for future systematic studies, where the measurement approach described here could be used to complement real-time observations.

Figure 3 depicts a two-dimensional (2D) map illustrating the gas-particle partitioning of aerosolized PO₁ mixture, represented by a color gradient. This visualization is based on the constructed VBS distributions, considering a wide range of the tOM loadings from 0.1 to 1000 μ g m⁻³, and temperatures (T) ranging from 273 to 323 K. The degree of gas-particle partitioning exhibits a significant dependency on both tOM and T. Across the range of conditions considered, particle-phase mass fractions of PO₁ fluctuate from approximately 10% (at low tOM and high T) to around 90% (with high tOM and low T). A similar 2D map constructed for the PO₃ mixture is included in SI (Figure S6). The 2D maps enable a visual assessment of the atmospheric cooling rates, emission sources strength, and dilution effects on the gas-particle partitioning of organic components within aged biomass burning plumes. When original BBOA emissions are rapidly

cooled by the surrounding low temperature environment, the particle fraction initially rises and then decreases throughout the atmospheric dilution process, as depicted in Figure 3 by the blue-line trajectory. However, at warmer ambient temperatures, the particle-to-gas evaporation due to dilution may exceed the gas-to-particle condensation due to cooling, resulting in an overall slow progressive evaporation of species from the particle phase, as illustrated in Figure 3 by the red-line trajectory. Hence, the specific gas-solid distribution of organic compounds is affected by multiple factors, including rates of atmospheric cooling and dilution, as well as the temperature and strength of emission sources. Of note, extensive partitioning from particle to gas phase is particularly prominent when *tOM* loadings are at the level of 10 µg m⁻³ and below. This suggests that nascent BBOA particles serve as vital carriers of later gas-phase components, which will facilitate atmospheric gas-phase reactions and SOA formation⁵⁵ in pristine environments located downwind of the BBOA emission sources.

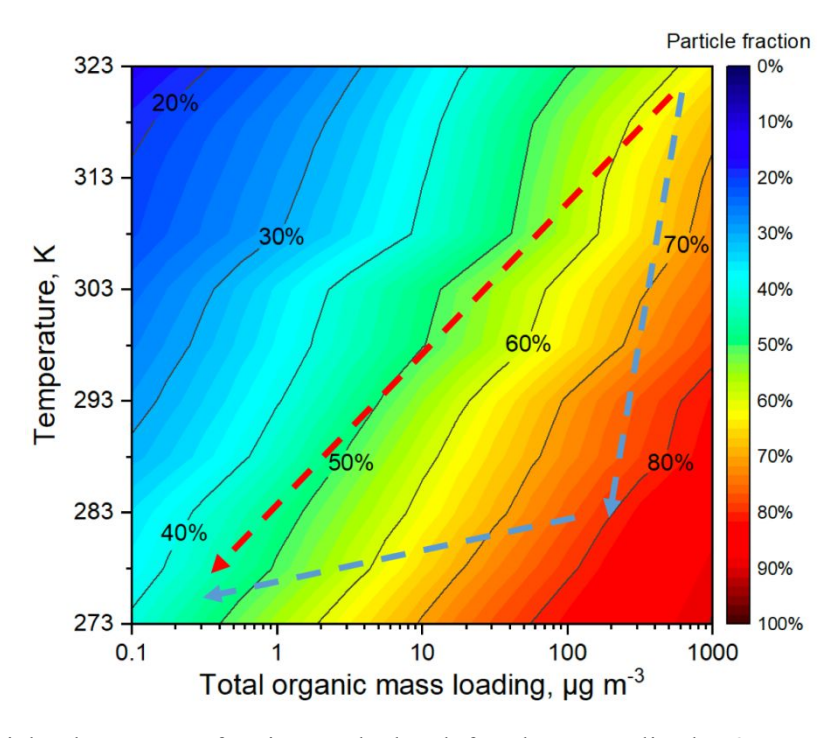


Figure 3. Particle-phase mass fractions calculated for the aerosolized PO₁ components using the constructed VBS distributions and considering broad ranges of ambient temperatures and total organic mass

(tOM) loadings. Dash lines showcase the rapid cooling trajectory (blue line) versus gradual cooling trajectory (red line).

The transition of individual components from particle to gas phases can be significantly impeded by transport limitations, particularly slow diffusion within the BBOA particles themselves, especially as they become more viscous and semi-solid. Notably, existing parameterization approaches^{32, 56} allow for the computation of viscosity values for all individual species identified in the TPD-DART-HRMS experiments. This information is then utilized to assess the apparent viscosity of particle-phase mixtures based on the mass contributions of individual species in the particle phase and the degree of gas-particle partitioning, both inferred from the VBS distributions. Figure 4 illustrates the VBS distributions of PO₁ and PO₃ mixtures combined with the componentspecific viscosity information, with individual bins color-coded to represent mass fractions of species with different viscosity ranges. Considering a viscosity value of 10³ Pa·s, equivalent to the viscosity of paraffin wax, as the boundary between liquid-like and semi-solid materials, 37, 57 kinetic limitations on the particle-to-gas-phase transition can be evaluated. The plots indicate that IVOC species have viscosity values less than 10³ Pa·s, indicating a liquid-like physical state. SVOC and LVOC species exhibit viscosity ranges of 10³–10⁷ Pa·s and 10⁶–10⁹ Pa·s, respectively, comparable to highly viscous waxes and semi-solid pitch material. ELVOC species have the highest viscosity of >10⁸ Pa·s, approaching the viscosity of solid vitreous carbon or amorphous glass.³⁷ Notably, if the characteristic mixing time (e-folding time) of BBOA components within individual particles exceeds tens of minutes, the atmospheric particle-to-gas partitioning may be substantially hindered by slow diffusion within the particles. Considering a typical diameter of 200 nm for BBOA particles, a threshold viscosity of >10⁵ Pa·s is derived using Eq. 9. At higher viscosities, diffusion within the particle phase becomes the critical limiting factor controlling the kinetics of the particle-to-gas partitioning. Additionally, temperature variations impact the

viscosity of BBOA compounds, inherently affecting diffusion and characteristic mixing times, as illustrated in Figure S7. For the specific conditions of tOM and T, the resulting viscosity of the particle-phase fractions of PO_x can be computed using Eqs 5–7, which require input values of the mass contributions of individual species (i) and their $T_{g,i}$ values.

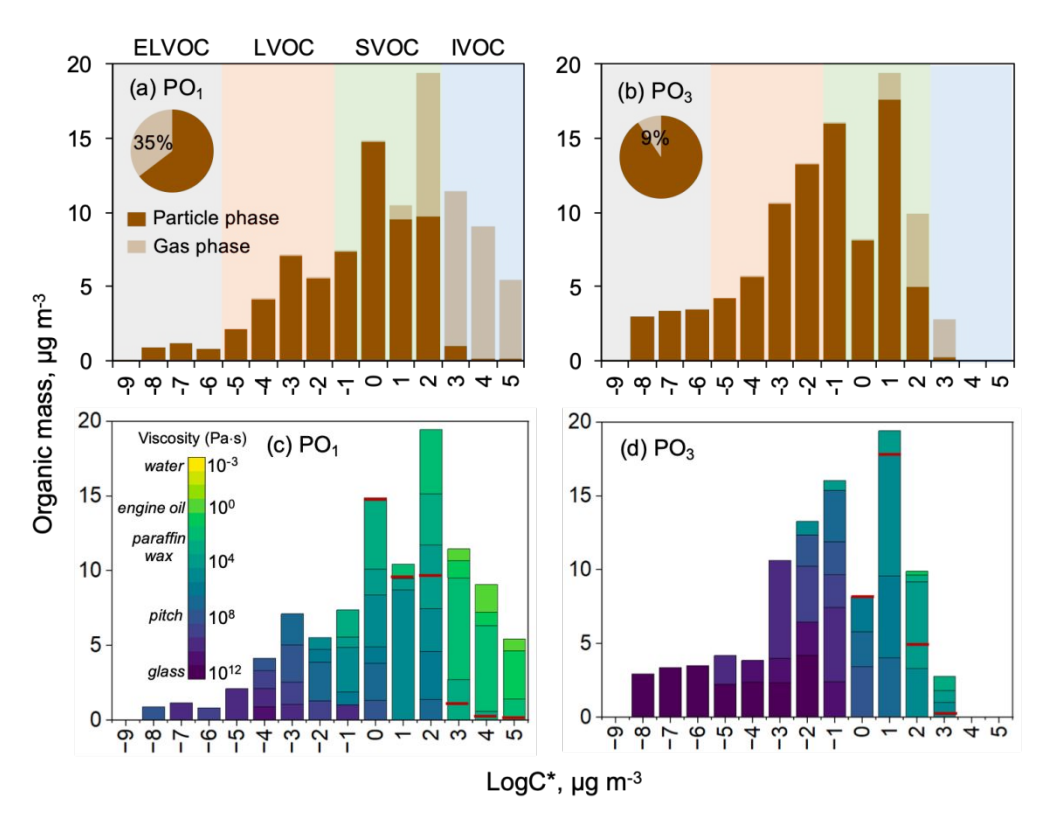


Figure 4. (a, b) Comparison of the VBS distributions constructed for PO_1 and PO_3 mixtures under conditions of T=298 K and tOM=100 μ g m⁻³. Pie charts depict the estimated mass fractions percent of total gas- and particle-phase species summed across all VBS bins. (c, d) The same VBS distributions as shown above, incorporating information on viscosity values calculated for individual components identified in the mixtures. The viscosity values of individual components are segmented into a series of groups with viscosity ranges that differ by a factor of 10. Each bin in the VBS distributions is color-coded to represent contributions of components with varying viscosity ranges. The color bar denotes the viscosity ranges, with reference materials indicated on the left.

To validate the feasibility of adequate viscosity prediction from the molecular characterization data discussed in this work, we compared the computed viscosity values for the PO_x bulk mixtures

with the corresponding experimental results measured in the poke-flow experiments. 58 Figure 5a displays the results of this comparison, showcasing the computed and experimentally measured viscosity values at 298K for a series of PO_x mixtures prepared through controlled evaporation in laboratory experiments. The viscosities of PO₁, PO_{1,33}, PO₂, and PO₃ mixtures computed based on the elemental formulas and VTF equation ^{32, 33} were 10^{3,2}, 10^{5,0}, 10^{7,9}, and 10^{9,3} Pa·s; viscosities calculated from the C^*_{298K} values³⁸ were $10^{3.3}$, $10^{5.1}$, $10^{7.8}$, and $10^{8.9}$ Pa·s, increasing significantly as the volume of PO_x decreases upon evaporation. The measured viscosity values were consistent with the computed results. The measured viscosity of PO₁ mixture was at the lower limit of 10³ Pa·s. The measured viscosity increased as the volume of the PO_x mixtures decreased, with the measured viscosity of $PO_{1.3\pm0.1}$ and $PO_{1.8\pm0.1}$ corresponding to $10^{5.1\pm0.4}$ Pa·s and $10^{7.7\pm0.1}$, respectively. The measured viscosity of the $PO_{2.9\pm0.9}$ mixture approached the upper measurement limit of >108 Pa·s, where the poked droplets shatter and no relaxation flow can be observed. Both computed and measured results indicate a significant rise in viscosity increase across several orders of magnitude during non-reactive evaporation. While the glass transition temperatures, $T_g(\omega_{org})$, of PO_r mixtures may be influenced by variable matrix effects unique to each mixture, and the use of a single Gordon-Taylor constant in eq. 6 is a simplified approach, the close agreement between the calculated results and poke-flow measurements validates its practical applicability.

The consistent viscosity trend over the set of PO_x mixtures not only demonstrates the utility of the viscosity predictions based on the chemical characterization data from the TPD-DART-HRMS experiments, but also provides means for quantitative assessment of the evaporation processes on the viscosity of atmospheric BBOA. Previous studies have shown that particles collected near a fire, characterized as fresh BB aerosols, exhibit low viscosity. However, as they age within the smoke plume, their viscosities increase significantly, often resulting in the formation of spherical

semi-solid (glassy) particles commonly referred to as 'tar balls'.^{52,59} Our work illustrates that when half of the volume of BBOA evaporates (from PO₁ to PO₂), their viscosity increases by four orders of magnitude, potentially resulting in the amorphous semi-solid tar balls. Such drastic viscosity changes can also hinder particle-to-gas transitions through lowering the molecular diffusion rates of BBOA components.⁶⁰

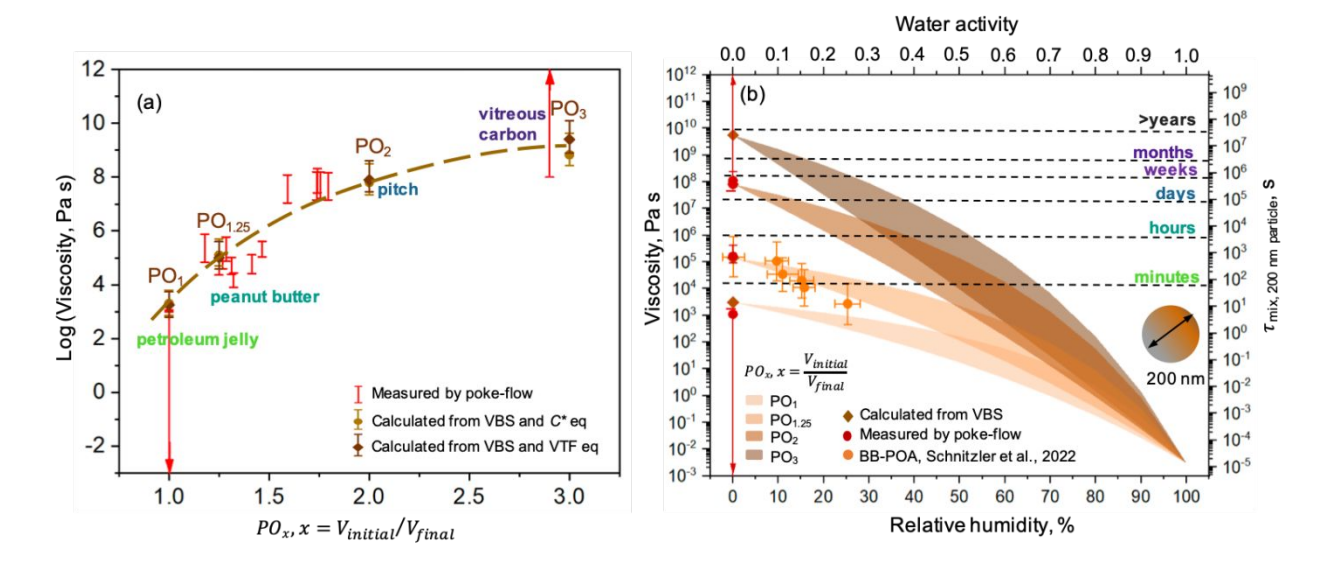


Figure 5. (a) The comparison of viscosity values computed for PO_x mixtures based on the constructed VBS distributions and $T_g(\omega_{org})$ values derived from elemental formulas and VTF equation^{32, 33}, those derived from C^* values³⁸ and experimental viscosity values derived from the poke-flow measurements conducted at room temperature. The dashed line in the plot indicates a polynomial fit of the computed PO_x viscosity values, parameterized as $\log(\eta) = 1.39x^2 + 8.56x - 3.90$ (R² = 0.99). (b) Viscosity and *e*-folding times computed for 200 nm particles composed of PO_x mixtures and water content equilibrated at different levels of RH at room temperature.

The viscosity and diffusion in BBOA particles are significantly influenced by their water content equilibrated with external relative humidity (RH),^{33, 61, 62} which can be further quantified for aerosolized PO_x mixtures based on literature reported effective hygroscopicity parameter of κ = 0.057±0.07 for BBOA particles.³⁵ Figure 5b illustrates the results of these calculations for particles composed of each of the four PO_x mixtures, showcasing variations in their viscosity predicted for

different atmospheric RH conditions at 298K. Elevated water activity decreases the viscosity of BBOA, and this impact becomes more pronounced as the degree of evaporation (x) increases. Additionally, it is expected that the hygroscopicity of PO_x would decreases substantially with increasing x values, and therefore PO₃ may become hydrophobic with κ approaching 0. Figure S8 showcases variations in viscosity of PO_x mixtures as a function of RH, where variable κ values of 0.15, 0.10, 0.05, and 0.02 were assigned for PO₁, PO_{1,33}, PO₂, and PO₃, respectively. As the degree of evaporation (x) increases, the viscosity of BBOA remains rather unchanged at RH<40% but exhibits more noticeable variations at higher RH. When the viscosity of BBOA increases to a significant level, such as 10⁹ Pa·s of PO₃, PO_r likely remains nearly hydrophobic at relatively low RH. Furthermore, as illustrated in Figure S9, lower tOM loadings and colder temperatures also increase the viscosity and e-folding time of BBOA. These findings underscore the significant influence environmental conditions, such as temperatures, RH, and tOM loadings during atmospheric dilution, on the viscosity and diffusion within condensed phase of BBOA during transport. In particular, lower temperatures, reduced RH, and the dilution process collectively contribute to an increase in BBOA viscosity.

The viscosity of BBOA undergoes significant changes caused by evaporation during atmospheric transportation. As illustrated in Figures 4c and 4d, there is a notable increase in the contribution of highly viscous species in the PO₃ sample, compared to PO₁. In PO₃, the liquid-like species with viscosity values less than 10³ Pa·s are largely depleted, while the highly viscous semisolid species persist, particularly those with viscosity values exceeding 10⁸ Pa·s, comparable to pitch tar.³⁷ As indicated in Figure S10, the PO₃ mixture exhibits substantially higher viscosity compared to PO₁ under identical environmental conditions, including *tOM* loadings, temperatures, and RH. These findings suggest that as BBOA particles gradually evaporate in emission plumes

due to atmospheric dilution, their low-viscosity components vaporize, leaving behind highviscosity components, and leading to the solidification of aged BBOA particles, commonly referred to as tar balls. Additionally, the condensed-phase reactions inside particles may also lead to the formation of oligomers, contributing to the increased viscosity of PO₃. This solidification significantly impedes condensed-phase diffusion, resulting in much longer characteristic e-folding mixing times of species equilibrating within the particles. Considering 200 nm as a typical diameter for BBOA particles and assuming that fresh and aged particles are represented by the PO₁ and PO₃ proxies, respectively, trends in their characteristic mixing times can be evaluated. Specifically, as PO₁ transforms into PO₃ upon evaporation, the viscosity of BBOA particles would change from 10³ Pa·s to 10⁸ Pa·s under dry conditions, corresponding to changes in mixing times from seconds to months. At more atmospherically relevant conditions of 50–60% RH, the viscosity of BBOA particles may range from 10¹ Pa·s to 10⁵ Pa·s, still significant enough to slow down mixing times from milliseconds to hours. Lower atmospheric temperatures of BBOA plumes from wildfires transported aloft would further facilitate solidification, leading to the formation of tar balls as illustrated in Figures S10 and S11. Electron microscopy imaging of individual BBOA particles sampled during aircraft transects at varying distances downwind from a wildland fire revealed that tar balls form within approximately three hours of ageing, driven by transformation and solidification of the initially emitted liquid-like particles.^{52, 59} These studies reported a significant increase in tar ball mass fractions, rising from less than 1% near the fire to 31–45% downwind,⁵² and an increase in tar ball number fractions from nearly zero in young smoke to approximately 80% in aged smoke.⁵⁹ While atmospheric aging of BBOA is synergistically influenced by both reactive chemistry and physical processes. 63, 64 the evaporation of semi-volatile components from particles alone can significantly contribute their solidification. Under consistent

environmental conditions of 283–288 K and 40–50% RH, the viscosity of fresh BBOA particles is 10^2 – 10^3 Pa·s, but rapidly increases to 10^9 – 10^{10} Pa·s in aged BBOA particles, supporting tar ball formation. During atmospheric transport, as tOM loading decreases from ~1000 µg m⁻³ to ~100 µg m⁻³ or less, the viscosity of BBOA particles increases from 10^2 to 10^9 Pa·s, highlighting the role of evaporation in this transformation. It is important to note that humidity-driven hydration and dehydration effects can lead to irreversible particle transformations, which are not accounted for in the estimated values presented above. The resulting uncertainty in composition and optical properties of the real-world BBOA particles due to humidity fluctuations should also be considered. Furthermore, variability in the mixing states of BBOA particle ensembles may introduce additional complexity to the effects of volatilization.

ATMOSPHERIC IMPLICATIONS

The atmospheric aging of BBOA involves a series of physical and chemical transformations, with evaporation and solidification playing a pivotal role. Understanding the impact of evaporation on BBOA is essential for assessing its broader implications on atmospheric chemistry and climate. During atmospheric transport, evaporation prompts highly volatile and low-viscosity compounds to transition into the gas phase. Consequently, compounds with low volatility, high viscosity, and stronger light-absorbing properties remain in BBOA, enhancing the BrC absorption and thereby affecting climate. The TPD-DART-HRMS measurement platform offers unique capability to measure the apparent volatility of individual compounds, enabling the acquisition of valuable temperature-dependent volatility profiles of complex mixtures. This advancement facilitates the quantification of solid-gas partitioning and viscosity under varying environmental conditions. Specifically, our results indicate that BBOA typically undergoes a process of becoming more

viscous during regional or vertical transport in the atmosphere. This increase in viscosity can prolong the atmospheric lifetimes of various BBOA components, thus amplifying their impact on radiative forcing and air quality. 65-67 Additionally, the enhanced viscosity of BBOA can facilitate their propensity to act as cloud ice nuclei. 68 Importantly, the gas-particle partitioning of BBOA throughout its atmospheric transport is highly sensitive to environmental conditions. Our study demonstrates how variations in temperature and atmospheric mass loadings may influence the gasparticle partitioning of BBOA particles, leading to significant alternations in their viscosity and optical properties. Furthermore, our study provides quantitative insights into the origin and formation mechanism of the highly viscous tar ball particles commonly observed in aged biomass burning emissions. 52, 59, 69 We suggest that tar balls form through the solidification of BBOA particles upon the evaporation of their semi volatile components. We emphasize the profound influence of environmental conditions, such as humidity, on these transformations. However, the aging of atmospheric BrC involves not only volatilization but also other processes such as photochemical aging and oxidation. Future research should explore the combined effects of these aging mechanisms, as they have distinct impacts on BBOA.

ASSOCIATED CONTENT

Supporting Information

The following supporting information is available free of charge.

Additional information as mentioned in the text; Volatility basis sets constructions, viscosity calculations and viscosity measurements, Progression of TPD-DART-HRMS spectra and molecular characteristics of PO_x samples, The comparison of VBS distribution of PO_x mixtures with literature ones, Gas-particle partitioning of PO_1 mixtures under variable T and tOM

- conditions, VBS distributions and viscosity of PO_1 mixtures under variable T conditions, Viscosity and e-folding time of PO_x mixtures as a function of RH under variable T and tOM conditions (Supplemental Notes S1–S6); additional Text S1, Figures S1–S11, and Table S1 illustrating supplemental notes (PDF).
- VBS distribution template of PO_x mixtures (XLSX).
- 552 AUTHOR INFORMATION
- 553 Corresponding Author
- * e-mail: alaskin@purdue.edu
- 555 Notes

The authors declare no competing financial interest.

ACKNOWLEDGMENT

The PU group acknowledges support by the U.S. National Oceanic and Atmospheric Administration Grant NA22OAR4310195. Preparation of PO_x samples and their characterization using auxiliary measurement methods were performed with support by the international collaboration grant from US National Science Foundation (NSF Grant no. AGS-2039985), US-Israel Binational Science Foundation (BSF Grant no. 2020656). The WIS group acknowledges additional support from the Israel Science Foundation (Grant no. 928/21). The UBC group acknowledges support from the Natural Sciences and Engineering Research Council of Canada, (NSERC Grant no. RGPIN-2023-05333).

2 3

4 5

6

7

8

REFERENCES

- 1. Laskin, A.; Laskin, J.; Nizkorodov, S. A., Chemistry of atmospheric brown carbon.
- 569 Chem. Rev. 2015, 115, (10), 4335.
- 570 2. Andreae, M. O.; Gelencsér, A., Black carbon or brown carbon? The nature of light-
- absorbing carbonaceous aerosols. *Atmos. Chem. Phys.* **2006**, *6*, (10), 3131-3148.
- 572 3. Jacobson, M. Z., Isolating nitrated and aromatic aerosols and nitrated aromatic gases as
- 573 sources of ultraviolet light absorption. *J. Geophys. Res.-Atmos.* **1999**, *104*, (D3), 3527-3542.
- 574 4. Chen, Q.; Chen, Q.; Hua, X.; Guan, D.; Chang, T., Gas-phase brown carbon: Absorbance
- 575 and chromophore types. *Atmos. Environ.* **2021,** *264*, 118646.
- 576 5. Saleh, R., From measurements to models: toward accurate representation of brown
- 577 carbon in climate calculations. *Current Pollution Reports* **2020**, *6*, 90-104.
- 578 6. Brown, H.; Liu, X.; Pokhrel, R.; Murphy, S.; Lu, Z.; Saleh, R.; Mielonen, T.; Kokkola,
- H.; Bergman, T.; Myhre, G., Biomass burning aerosols in most climate models are too
- 580 absorbing. *Nat. Commun.* **2021,** *12*, (1), 277.
- 7. Palm, B. B.; Peng, Q.; Fredrickson, C. D.; Lee, B. H.; Garofalo, L. A.; Pothier, M. A.;
- Kreidenweis, S. M.; Farmer, D. K.; Pokhrel, R. P.; Shen, Y., Quantification of organic aerosol
- and brown carbon evolution in fresh wildfire plumes. *Proc. Natl. Acad. Sci. USA* **2020,** *117*,
- 584 (47), 29469-29477.
- 585 8. Farley, R.; Bernays, N.; Jaffe, D. A.; Ketcherside, D.; Hu, L.; Zhou, S.; Collier, S.;
- Zhang, Q., Persistent Influence of Wildfire Emissions in the Western United States and
- 587 Characteristics of Aged Biomass Burning Organic Aerosols under Clean Air Conditions.
- 588 Environ. Sci. Technol. **2022**, *56*, (6), 3645-3657.
- Hems, R. F.; Schnitzler, E. G.; Liu-Kang, C.; Cappa, C. D.; Abbatt, J. P., Aging of
- atmospheric brown carbon aerosol. ACS Earth and Space Chemistry 2021, 5, (4), 722-748.
- 591 10. Sedlacek III, A. J.; Lewis, E. R.; Onasch, T. B.; Zuidema, P.; Redemann, J.; Jaffe, D.;
- 592 Kleinman, L. I., Using the black carbon particle mixing state to characterize the lifecycle of
- 593 biomass burning aerosols. *Environ. Sci. Technol.* **2022**, *56*, (20), 14315-14325.
- 594 11. Calderon-Arrieta, D.; Morales, A. C.; Hettiyadura, A. P. S.; Estock, T. M.; Li, C.;
- Rudich, Y.; Laskin, A., Enhanced Light Absorption and Elevated Viscosity of Atmospheric
- Brown Carbon through Evaporation of Volatile Components. *Environ. Sci. Technol.* **2024,** *58*,
- 597 (17), 7493–7504.
- 598 12. Hettiyadura, A. P. S.; Garcia, V.; Li, C.; West, C. P.; Tomlin, J.; He, Q.; Rudich, Y.;
- Laskin, A., Chemical composition and molecular-specific optical properties of atmospheric
- brown carbon associated with biomass burning. *Environ. Sci. Technol.* **2021**, *55*, (4), 2511-2521.
- 601 13. Pöschl, U.; Shiraiwa, M., Multiphase Chemistry at the Atmosphere–Biosphere Interface
- Influencing Climate and Public Health in the Anthropocene. *Chem. Rev.* **2015**, *115*, (10), 4440-
- 603 4475.
 - 604 14. Abbatt, J. P.; Ravishankara, A. R., Opinion: Atmospheric multiphase chemistry–past,
 - 605 present, and future. *Atmos. Chem. Phys.* **2023**, *23*, (17), 9765-9785.
- 606 15. Pagonis, D.; Selimovic, V.; Campuzano-Jost, P.; Guo, H.; Day, D. A.; Schueneman, M.
- 607 K.; Nault, B. A.; Coggon, M. M.; DiGangi, J. P.; Diskin, G. S., Impact of biomass burning

58 59

- organic aerosol volatility on smoke concentrations downwind of fires. *Environ. Sci. Technol.*
- 609 **2023**, *57*, (44), 17011-17021.
- 16. Donahue, N. M.; Kroll, J.; Pandis, S. N.; Robinson, A. L., A two-dimensional volatility
- basis set–Part 2: Diagnostics of organic-aerosol evolution. *Atmos. Chem. Phys.* **2012**, *12*, (2),
- 612 615-634.
- 17. Isaacman-VanWertz, G.; Massoli, P.; O'Brien, R.; Lim, C.; Franklin, J. P.; Moss, J. A.;
- Hunter, J. F.; Nowak, J. B.; Canagaratna, M. R.; Misztal, P. K., Chemical evolution of
- atmospheric organic carbon over multiple generations of oxidation. *Nature Chem.* **2018,** *10*, (4),
- 14 616 462-468.
 - 18. Lopez-Hilfiker, F.; Mohr, C.; D'ambro, E.; Lutz, A.; Riedel, T.; Gaston, C.; Iyer, S.;
 - Zhang, Z.; Gold, A.; Surratt, J., Molecular composition and volatility of organic aerosol in the
 - 619 Southeastern US: implications for IEPOX derived SOA. *Environ. Sci. Technol.* **2016**, *50*, (5),
- 19 620 2200-2209.
 - 621 19. Gao, L.; Buchholz, A.; Li, Z.; Song, J.; Vallon, M.; Jiang, F.; Möhler, O.; Leisner, T.;
 - Saathoff, H., Volatility of Secondary Organic Aerosol from β-Caryophyllene Ozonolysis over a
 - Wide Tropospheric Temperature Range. Environ. Sci. Technol. 2023, 57, (24), 8965-8974.
 - 424 20. Ye, Q.; Wang, M.; Hofbauer, V.; Stolzenburg, D.; Chen, D.; Schervish, M.; Vogel, A.;
 - Mauldin, R. L.; Baalbaki, R.; Brilke, S., Molecular composition and volatility of nucleated
 - particles from α-pinene oxidation between 50 C and + 25 C. Environ. Sci. Technol. 2019, 53,
 - 627 (21), 12357-12365.
 - 628 21. Surdu, M.; Lamkaddam, H.; Wang, D. S.; Bell, D. M.; Xiao, M.; Lee, C. P.; Li, D.;
 - 629 Caudillo, L.; Marie, G.; Scholz, W., Molecular Understanding of the Enhancement in Organic
 - Aerosol Mass at High Relative Humidity. *Environ. Sci. Technol.* **2023**, *57*, (6), 2297-2309.
 - 631 22. Ortiz-Montalvo, D. L.; Häkkinen, S. A.; Schwier, A. N.; Lim, Y. B.; McNeill, V. F.;
 - Turpin, B. J., Ammonium addition (and aerosol pH) has a dramatic impact on the volatility and
 - yield of glyoxal secondary organic aerosol. *Environ. Sci. Technol.* **2014,** *48*, (1), 255-262.
 - West, C. P.; Hsu, Y.-J.; MacFeely, K. T.; Huston, S. M.; Aridjis-Olivos, B. P.; Morales,
 - A. C.; Laskin, A., Volatility Measurements of Individual Components in Organic Aerosol
 - 636 Mixtures Using Temperature-Programmed Desorption–Direct Analysis in Real Time–High
 - 637 Resolution Mass Spectrometry. *Anal. Chem.* **2023**, *95*, (19), 7403-7408.
 - 638 24. Xie, Q.; Halpern, E. R.; Zhang, J.; Shrivastava, M.; Zelenyuk, A.; Zaveri, R. A.; Laskin,
 - 639 A., Volatility Basis Set Distributions and Viscosity of Organic Aerosol Mixtures: Insights from
 - 640 Chemical Characterization Using Temperature-Programmed Desorption–Direct Analysis in
 - Real-Time High-Resolution Mass Spectrometry. Anal. Chem. 2024, 96, (23), 9524-9534.
 - 42 25. Ye, Q.; Robinson, E. S.; Ding, X.; Ye, P.; Sullivan, R. C.; Donahue, N. M., Mixing of
 - secondary organic aerosols versus relative humidity. *Proc. Natl. Acad. Sci. USA* **2016,** *113*, (45),
 - 644 12649-12654.
 - Petters, S. S.; Kreidenweis, S. M.; Grieshop, A. P.; Ziemann, P. J.; Petters, M. D.,
 - Temperature and humidity dependent phase states of secondary organic aerosols. *Geophys.*
 - 647 Res. Lett. **2019**, 46, (2), 1005-1013.

- Reid, J. P.; Bertram, A. K.; Topping, D. O.; Laskin, A.; Martin, S. T.; Petters, M. D.;
- Pope, F. D.; Rovelli, G., The viscosity of atmospherically relevant organic particles. *Nat.*
- *Commun.* **2018,** *9*, (1), 956.
- 651 28. Li, C.; He, Q.; Schade, J.; Passig, J.; Zimmermann, R.; Meidan, D.; Laskin, A.; Rudich,
- Y., Dynamic changes in optical and chemical properties of tar ball aerosols by atmospheric
- 653 photochemical aging. *Atmos. Chem. Phys.* **2019**, *19*, (1), 139-163.
- Roach, P. J.; Laskin, J.; Laskin, A., Higher-order mass defect analysis for mass spectra of
- 655 complex organic mixtures. *Anal. Chem.* **2011**, *83*, (12), 4924-4929.
 - 656 30. Chattopadhyay, S.; Tobias, H. J.; Ziemann, P. J., A method for measuring vapor
- pressures of low-volatility organic aerosol compounds using a thermal desorption particle beam
- 658 mass spectrometer. *Anal. Chem.* **2001,** *73,* (16), 3797-3803.
- 659 31. Donahue, N. M.; Epstein, S. A.; Pandis, S. N.; Robinson, A. L., A two-dimensional
 - volatility basis set: 1. organic-aerosol mixing thermodynamics. Atmos. Chem. Phys. 2011, 11,
 - 661 (7), 3303-3318.
 - 662 32. DeRieux, W.-S. W.; Li, Y.; Lin, P.; Laskin, J.; Laskin, A.; Bertram, A. K.; Nizkorodov,
- S. A.; Shiraiwa, M., Predicting the glass transition temperature and viscosity of secondary
- organic material using molecular composition. *Atmos. Chem. Phys.* **2018**, *18*, (9), 6331-6351.
- 665 33. Galeazzo, T.; Valorso, R.; Li, Y.; Camredon, M.; Aumont, B.; Shiraiwa, M., Estimation
- of secondary organic aerosol viscosity from explicit modeling of gas-phase oxidation of isoprene
- and α-pinene. Atmos. Chem. Phys. 2021, 21, (13), 10199-10213.
- 668 34. Petters, M.; Kreidenweis, S., A single parameter representation of hygroscopic growth
 - and cloud condensation nucleus activity. *Atmos. Chem. Phys.* **2007**, *7*, (8), 1961-1971.
- 670 35. Bougiatioti, A.; Bezantakos, S.; Stavroulas, I.; Kalivitis, N.; Kokkalis, P.; Biskos, G.;
- Mihalopoulos, N.; Papayannis, A.; Nenes, A., Biomass-burning impact on CCN number,
- 672 hygroscopicity and cloud formation during summertime in the eastern Mediterranean. *Atmos.*
- *Chem. Phys.* **2016**, *16*, (11), 7389-7409.
- 674 36. Dette, H. P.; Qi, M.; Schröder, D. C.; Godt, A.; Koop, T., Glass-forming properties of 3-
- 675 methylbutane-1, 2, 3-tricarboxylic acid and its mixtures with water and pinonic acid.
- 676 J. Phys. Chem. A **2014**, 118, (34), 7024-7033.
- 677 37. Koop, T.; Bookhold, J.; Shiraiwa, M.; Pöschl, U., Glass transition and phase state of
- 678 organic compounds: dependency on molecular properties and implications for secondary organic
- 679 aerosols in the atmosphere. *Phys. Chem. Chem. Phys.* **2011**, *13*, (43), 19238-19255.
- 580 38. Zhang, Y.; Nichman, L.; Spencer, P.; Jung, J. I.; Lee, A.; Heffernan, B. K.; Gold, A.;
- Zhang, Z.; Chen, Y.; Canagaratna, M. R., The cooling rate-and volatility-dependent glass-
- forming properties of organic aerosols measured by broadband dielectric spectroscopy. *Environ.*
- *Sci. Technol.* **2019**, *53*, (21), 12366-12378.
- 684 39. Evoy, E.; Maclean, A. M.; Rovelli, G.; Li, Y.; Tsimpidi, A. P.; Karydis, V. A.; Kamal, S.;
- Lelieveld, J.; Shiraiwa, M.; Reid, J. P., Predictions of diffusion rates of large organic molecules
- in secondary organic aerosols using the Stokes–Einstein and fractional Stokes–Einstein relations.
- 687 Atmos. Chem. Phys. **2019**, *19*, (15), 10073-10085.

- 688 40. Seinfeld, J. H.; Pandis, S. N., *Atmospheric chemistry and physics: from air pollution to climate change.* John Wiley & Sons: 2016.
- 690 41. Grayson, J.; Song, M.; Sellier, M.; Bertram, A., Validation of the poke-flow technique
- combined with simulations of fluid flow for determining viscosities in samples with small
- 692 volumes and high viscosities. *Atmos. Meas. Tech.* **2015**, *8*, (6), 2463-2472.
- 693 42. Renbaum-Wolff, L.; Grayson, J. W.; Bateman, A. P.; Kuwata, M.; Sellier, M.; Murray,
- B. J.; Shilling, J. E.; Martin, S. T.; Bertram, A. K., Viscosity of α-pinene secondary organic
- material and implications for particle growth and reactivity. *Proc. Natl. Acad. Sci. USA* **2013**,
- *110*, (20), 8014-8019.
- 697 43. Smith, N. R.; Crescenzo, G. V.; Huang, Y.; Hettiyadura, A. P.; Siemens, K.; Li, Y.;
- Faiola, C. L.; Laskin, A.; Shiraiwa, M.; Bertram, A. K., Viscosity and liquid–liquid phase
- separation in healthy and stressed plant SOA. *Environmental Science: Atmospheres* **2021**, *1*, (3),
- 700 140-153.
 - 701 44. Tasoglou, A.; Louvaris, E.; Florou, K.; Liangou, A.; Karnezi, E.; Kaltsonoudis, C.;
- Wang, N.; Pandis, S. N., Aerosol light absorption and the role of extremely low volatility organic
- 703 compounds. Atmos. Chem. Phys. **2020**, 20, (19), 11625-11637.
- 704 45. Zhang, Y.; Su, H.; Kecorius, S.; Ma, N.; Wang, Z.; Sun, Y.; Zhang, Q.; Pöschl, U.;
- Wiedensohler, A.; Andreae, M. O., Extremely low-volatility organic coating leads to
- underestimation of black carbon climate impact. *One Earth* **2023**, *6*, (2), 158-166.
- 707 46. Cain, J.; Laskin, A.; Kholghy, M. R.; Thomson, M. J.; Wang, H., Molecular
- characterization of organic content of soot along the centerline of a coflow diffusion flame. *Phys.*
 - *Chem. Chem. Phys.* **2014**, *16*, (47), 25862-25875.
 - 710 47. Yang, L. H.; Takeuchi, M.; Chen, Y.; Ng, N. L., Characterization of thermal
 - decomposition of oxygenated organic compounds in FIGAERO-CIMS.
 - 712 Aerosol Sci. Technol. **2021**, *55*, (12), 1321-1342.
 - Huang, W.; Mohr, C.; Canagaratna, M.; Worsnop, D. R.; Valisirniö, A.; Huang, W.; Mohr, C.; Canagaratna, M.; Worsnop, D. R.;
 - Schobesberger, S.; Virtanen, A., Deconvolution of FIGAERO–CIMS thermal desorption profiles
 - using positive matrix factorisation to identify chemical and physical processes during particle
 - 716 evaporation. *Atmos. Chem. Phys.* **2020**, *20*, (13), 7693-7716.
 - 717 49. Stark, H.; Yatavelli, R. L.; Thompson, S. L.; Kang, H.; Krechmer, J. E.; Kimmel, J. R.;
 - 718 Palm, B. B.; Hu, W.; Hayes, P. L.; Day, D. A., Impact of thermal decomposition on thermal
 - desorption instruments: advantage of thermogram analysis for quantifying volatility distributions
 - 720 of organic species. *Environ. Sci. Technol.* **2017**, *51*, (15), 8491-8500.
 - 50. Lopez-Hilfiker, F.; Mohr, C.; Ehn, M.; Rubach, F.; Kleist, E.; Wildt, J.; Mentel, T. F.;
 - Carrasquillo, A.; Daumit, K.; Hunter, J., Phase partitioning and volatility of secondary organic
 - aerosol components formed from α-pinene ozonolysis and OH oxidation: the importance of
 - accretion products and other low volatility compounds. *Atmos. Chem. Phys.* **2015**, *15*, (14),
 - 725 7765-7776.
 - 726 51. Donahue, N. M.; Robinson, A. L.; Trump, E. R.; Riipinen, I.; Kroll, J. H., Volatility and
 - aging of atmospheric organic aerosol. *Atmos. Aerosol Chem.* **2014**, 97-143.

- 52. Sedlacek III, A. J.; Buseck, P. R.; Adachi, K.; Onasch, T. B.; Springston, S. R.;
- Kleinman, L., Formation and evolution of tar balls from northwestern US wildfires. *Atmos.*
- *Chem. Phys.* **2018**, *18*, (15), 11289-11301.
- 731 53. Feng, T.; Wang, Y.; Hu, W.; Zhu, M.; Song, W.; Chen, W.; Sang, Y.; Fang, Z.; Deng,
- W.; Fang, H., Impact of aging on the sources, volatility, and viscosity of organic aerosols in
- 733 Chinese outflows. *Atmos. Chem. Phys.* **2023**, *23*, (1), 611-636.
- 734 54. Xu, W.; Chen, C.; Qiu, Y.; Li, Y.; Zhang, Z.; Karnezi, E.; Pandis, S. N.; Xie, C.; Li, Z.;
- 735 Sun, J.; Ma, N.; Xu, W.; Fu, P.; Wang, Z.; Zhu, J.; Worsnop, D. R.; Ng, N. L.; Sun, Y., Organic
 - aerosol volatility and viscosity in the North China Plain: contrast between summer and winter.
- 737 Atmos. Chem. Phys. **2021**, 21, (7), 5463-5476.
- 738 55. Fang, Z.; Li, C.; He, Q.; Czech, H.; Gröger, T.; Zeng, J.; Fang, H.; Xiao, S.; Pardo, M.;
- Hartner, E., Secondary organic aerosols produced from photochemical oxidation of secondarily
 - evaporated biomass burning organic gases: Chemical composition, toxicity, optical properties,
 - 741 and climate effect. *Environ. Int.* **2021**, *157*, 106801.
 - 56. Li, Y.; Day, D. A.; Stark, H.; Jimenez, J. L.; Shiraiwa, M., Predictions of the glass
- transition temperature and viscosity of organic aerosols from volatility distributions. *Atmos.*
 - *Chem. Phys.* **2020**, *20*, (13), 8103-8122.
 - 57. Shiraiwa, M.; Ammann, M.; Koop, T.; Pöschl, U., Gas uptake and chemical aging of
 - semisolid organic aerosol particles. *Proc. Natl. Acad. Sci. USA* **2011,** *108*, (27), 11003-11008.
 - 58. Schnitzler, E. G.; Gerrebos, N. G.; Carter, T. S.; Huang, Y.; Heald, C. L.; Bertram, A. K.;
 - Abbatt, J. P., Rate of atmospheric brown carbon whitening governed by environmental
 - 749 conditions. *Proc. Natl. Acad. Sci. USA* **2022**, *119*, (38), e2205610119.
 - 750 59. Adachi, K.; Sedlacek III, A. J.; Kleinman, L.; Springston, S. R.; Wang, J.; Chand, D.;
 - Hubbe, J. M.; Shilling, J. E.; Onasch, T. B.; Kinase, T., Spherical tarball particles form through
 - rapid chemical and physical changes of organic matter in biomass-burning smoke. *Proc. Natl.*
 - 753 Acad. Sci. USA **2019**, 116, (39), 19336-19341.
 - 754 60. Kuwata, M.; Martin, S. T., Phase of atmospheric secondary organic material affects its
 - 755 reactivity. *Proc. Natl. Acad. Sci. USA* **2012**, *109*, (43), 17354-17359.
 - 756 61. Evoy, E.; Kiland, K. J.; Huang, Y.; Schnitzler, E. G.; Maclean, A. M.; Kamal, S.; Abbatt,
 - J. P.; Bertram, A. K., Diffusion coefficients and mixing times of organic molecules in β-
 - caryophyllene secondary organic aerosol (SOA) and biomass burning organic aerosol (BBOA).
 - *ACS Earth and Space Chemistry* **2021**, *5*, (11), 3268-3278.
 - 760 62. Gregson, F. K.; Gerrebos, N. G.; Schervish, M.; Nikkho, S.; Schnitzler, E. G.; Schwartz,
 - 761 C.; Carlsten, C.; Abbatt, J. P.; Kamal, S.; Shiraiwa, M., Phase Behavior and Viscosity in
 - Biomass Burning Organic Aerosol and Climatic Impacts. *Environ. Sci. Technol.* **2023**, *57*, (39),
 - 763 14548-14557.
 - 63. Lee, A. K.; Willis, M. D.; Healy, R. M.; Wang, J. M.; Jeong, C.-H.; Wenger, J. C.; Evans,
 - 765 G. J.; Abbatt, J. P., Single-particle characterization of biomass burning organic aerosol (BBOA):
 - evidence for non-uniform mixing of high molecular weight organics and potassium. *Atmos.*
 - *Chem. Phys.* **2016**, *16*, (9), 5561-5572.

- 768 64. Budisulistiorini, S. H.; Chen, J.; Itoh, M.; Kuwata, M., Can online aerosol mass
- spectrometry analysis classify secondary organic aerosol (soa) and oxidized primary organic
- aerosol (opoa)? A case study of laboratory and field studies of indonesian biomass burning. ACS
- *Earth and Space Chemistry* **2021**, *5*, (12), 3511-3522.
- 772 65. Zelenyuk, A.; Imre, D.; Beránek, J.; Abramson, E.; Wilson, J.; Shrivastava, M., Synergy
- between secondary organic aerosols and long-range transport of polycyclic aromatic
- hydrocarbons. *Environ. Sci. Technol.* **2012,** *46,* (22), 12459-12466.
- 775 66. Lou, S.; Shrivastava, M.; Ding, A.; Easter, R. C.; Fast, J. D.; Rasch, P. J.; Shen, H.;
- Massey Simonich, S. L.; Smith, S. J.; Tao, S., Shift in Peaks of PAH Associated Health Risks
- From East Asia to South Asia and Africa in the Future. *Earth's Future* **2023**, *11*, (6),
- 778 e2022EF003185.
- Shrivastava, M.; Lou, S.; Zelenyuk, A.; Easter, R. C.; Corley, R. A.; Thrall, B. D.; Rasch,
 - P. J.; Fast, J. D.; Massey Simonich, S. L.; Shen, H., Global long-range transport and lung cancer
 - risk from polycyclic aromatic hydrocarbons shielded by coatings of organic aerosol. *Proc. Natl.*
 - *Acad. Sci. USA* **2017**, *114*, (6), 1246-1251.
 - 783 68. Wolf, M. J.; Zhang, Y.; Zawadowicz, M. A.; Goodell, M.; Froyd, K.; Freney, E.; Sellegri,
 - K.; Rösch, M.; Cui, T.; Winter, M., A biogenic secondary organic aerosol source of cirrus ice
 - nucleating particles. *Nat. Commun.* **2020,** *11*, (1), 4834.
 - 786 69. Adachi, K.; Dibb, J. E.; Katich, J. M.; Schwarz, J. P.; Guo, H.; Campuzano-Jost, P.;
 - Jimenez, J. L.; Peischl, J.; Holmes, C. D.; Crawford, J., Occurrence, abundance, and formation of
 - atmospheric tarballs from a wide range of wildfires in the western US. EGUsphere 2024, 2024,
 - 789 1**-30**.